Hypothetical Visible Bands of Advanced Meteorological Imager Onboard the Geostationary Korea Multi-Purpose Satellite -2A Using Data-To-Data Translation

Kyung-Hoon Han, Jae-Cheol Jang, Sumin Ryu, Eun-Ha Sohn, and Sungwook Hong

***Abstract*—True-color imagery of satellites provides various atmospheric and surface information for intuitive understanding and visualization. This article presents a conditional generative adversarial network method for generating daytime and nighttime hypothetical visible (VIS) bands of the advanced meteorological imager (AMI) sensor onboard the geostationary Korea multipurpose satellite. The AMI datasets in the form of albedo and brightness temperature (T_B) were normalized and denormalized between 0 and 1 data-to-data (D2D) translation. The D2D model was trained and tested using data pair of the albedos at AMI VIS bands and AMI infrared (IR) bands or T_B differences between two AMI IR bands. The constructed D2D model showed that the statistical results of bias, root-mean-square-error, and correlation coefficient between the observed and D2D-generated AMI VIS bands during daytime were −0.006 and 0.047 in albedo, and 0.941 for the blue band; −0.007 and 0.05 in albedo and 0.939 for the green band; −0.01 and 0.061 in albedo, and 0.917 for the red band, respectively. The proposed D2D method is being officially used by the Korea meteorological administration. Except for simulating desert areas as clouds at night, the D2D model demonstrated excellent performance, generating hypothetical AMI VIS bands at day and night. Consequently, this article could significantly contribute to the monitoring and understanding of meteorological phenomena over one-third of the Earth. Additionally, the method can be extended to other geostationary weather satellites, including Himawari-8, Fengyun-4A, meteosat third generation, and geostationary operational environmental satellites.**

***Index Terms*—Adversarial, advanced meteorological imager (AMI), conditional generative adversarial network (CGAN), geokompsat-2a, hypothetical visible band, satellite remote sensing.**

I. Introduction

THE importance of information on weather and climate change is increasing because of anthropogenic activities, including leisure, business, natural disaster relief, and military operations. Satellites are used for the global observation of the Earth's surface and atmosphere, and monitor global weather and climate change providing short- to long-term data for predictions. Weather satellites observe electromagnetic waves emitted, reflected, and scattered from the Earth, passing through its atmosphere.

In particular, geostationary meteorological satellites, provide data for weather analysis, natural disasters (e.g., typhoons, floods, and heavy rainfall), geophysical parameters (e.g., sea surface temperature), and long-term records of climate change [1], [2]. These satellites have relatively high spatiotemporal resolutions that provide high-quality the atmospheric and surface observations. Most geostationary weather satellites employ meteorological sensors with 14–16 spectral bands ranging from visible (VIS) to infrared (IR), a spatial resolution of 2 km at nadir for the IR channels, and a temporal resolution of 10 min for full-disk (FD) observation [3], [4]. Geostationary Operational Environmental Satellite (GOES)-16 [3], Himawari-8 [4], Fengyun-4A (FY-4A) [5], Meteosat Third Generation (MTG) [6], and Geostationary Korea Multi-Purpose Satellite-2 Atmosphere (GK-2A) [7] are representative geostationary weather satellites.

In December 2018, the GK-2A, developed by the Korea Aerospace Research Institute and National Meteorological Satellite Center (NMSC) of the Korea Meteorological Administration (KMA), was launched on December 5, 2018, and equipped with an advanced meteorological imager (AMI) sensor with 16 bands from VIS to IR wavelengths as a successor of the communication, ocean, and meteorological satellite (COMS) [8] for meteorological purposes [9]. The AMI sensor began operating on July 25, 2019. GK-2A/AMI level (L) 1B products have a spatial resolution of 0.5–2 km and a temporal resolution of 10 min, and provide near real-time observations. NMSC/KMA

Manuscript received 15 June 2022; revised 28 July 2022 and 5 September 2022; accepted 23 September 2022. Date of publication 28 September 2022; date of current version 6 October 2022. This work was supported in part by the National Institute of Environment Research, in part by the Ministry of Environment of the Republic of Korea under Grant NIER-2021-01-01-052 and Grant NIER-2022-01-02-096, in part by the Korea Meteorological Administration Research and Development Program "Developing AI Technology for Weather Forecasting" under Grant KMA2021-00121, and in part by the "Technical Development on Weather Forecast Support and Convergence Service using Meteorological Satellites" under Grant KMA2020-00120. *(Corresponding author: Sungwook Hong.)*

Kyung-Hoon Han and Sumin Ryu are with the Department of Environment, Energy and Geoinformatics, Sejong University, Seoul 05006, South Korea (e-mail: khoon0798@sju.ac.kr; ryusm26@sju.ac.kr).

Jae-Cheol Jang and Eun-Ha Sohn are with the National Meteorological Satellite Center, Korea Meteorological Administration, Jincheon 27803, South Korea (e-mail: jaecheol00@korea.kr; soneh0431@korea.kr).

Sungwook Hong is with the Department of Environment, Energy and Geoinformatics, Sejong University, Seoul 05006, South Korea, and also with the DeepThoTh Co., Ltd., Seoul 05006, South Korea (e-mail: sesttiya@gmail.com).

Digital Object Identifier 10.1109/JSTARS.2022.3210143

has developed various L2 and L3 products using GK-2A/AMI L1B [10], [11].

The VIS band image represents the intensity of sunlight reflected from the Earth and cloud surfaces. In these images, oceans appear dark, whereas clouds appear bright [12]. Therefore, VIS bands are useful for cloud observation. True-color imagery based on the red, green, and blue (RGB) VIS bands in satellites helps capture various atmospheric and surface information because of its intuitive understanding, visualization, and lack of observational data loss [13]. However, despite the advantages of VIS band images, various satellite remote sensing studies have presented difficulties in discriminating fog from clouds [14] mainly because fog generally develops at night or in predawn hours [15] when VIS band images are unavailable owing to the absence of solar reflection [16].

Apart from the development of geostationary weather satellites, recent efforts have been made to combine deep learning (DL) and machine learning (ML) with big data, with increase in computing power owing to the development of graphics processing units (GPUs). The rapid growth of digital data has created transformative potential in various scientific data-driven studies [17] using artificial neural networks [18]. Numerous studies utilizing satellite data have demonstrated the effectiveness of the ML and DL methods [19]. The state-of-the-art DL techniques, such as convolutional neural networks (CNNs) [20], [21], convolutional long short-term memory [22], and conditional generative adversarial networks (cGANs) [23], [24], [25], [26], [27], [28], [29], have been used in various satellite remote sensing studies [30], [31], [32], [33]. DL techniques have shown to overcome the limitations of traditional approaches of satellite observations.

Several ML and DL techniques combined with the Korean geostationary weather satellites have been studied for hourly surface solar irradiance using CNN [34]. These include monitoring the overshooting tops in convective clouds related to severe weather events, such as lightning, hail, and heavy rainfall using 2D- and 3D-CNN [35]; improving thunderstorm detection method using an ML-based logistic regression method with GK-2A/AMI, ground radars, lightning, and numerical model data [36]; virtual nighttime VIS image generation using cGAN with single [31] or multiple [16] bands observation data from the Meteorological Imager (MI) sensor of the COMS satellite; and simulating nighttime reflectance and daytime radiance of the COMS/MI 3.75 μm band using the CGAN method [32].

This article presents a DL method based on data-to-data (D2D) translation to simulate hypothetical GK-2A/AMI VIS bands and provide virtual AMI RGB images using the observed AMI IR bands and band differences during the day and night. The cGAN technique using Pix2Pix software [37] was adopted to simulate the virtual VIS bands of the GK-2A/AMI sensor by a DL model trained and tested using pairs of GK-2A/AMI VIS bands with AMI IR bands and differences in IR bands. Virtual AMI VIS bands do not require solar reflection, and can be generated by the D2D model constructed by an adversarial task using cGAN. The D2D-simulated AMI VIS bands could complement the various uses of AMI sensors for atmospheric and meteorological purposes and be helpful for operational forecasters and analysts.

TABLE I
CHARACTERISTICS OF THE AMI SPECTRAL BANDS

Band number	Central Wavelength (μm)	Spatial Resolution (km)	Physical Properties
1	0.47	1	Vegetation, aerosol
2	0.51	1	Vegetation, aerosol
3	0.64	0.5	Low cloud, fog
4	0.86	1	Vegetation, aerosol
5	1.37	2	Cloud phase
6	1.6	2	Particle size
7	3.8	2	Low cloud, fog, forest fire
8	6.3	2	Mid- and upper-level moisture
9	6.9	2	Mid-level moisture
10	7.3	2	Mid- and lower-level moisture
11	8.7	2	Cloud phase, SO2
12	9.6	2	Ozone content
13	10.5	2	Cloud imagery, information of cloud top
14	11.2	2	Cloud imagery, sea surface temperature
15	12.3	2	Cloud imagery, sea surface temperature
16	13.3	2	Cloud top height, CO2

II. DATA

A. Satellite Data and Study Area

This article used AMI data containing three VIS (0.47, 0.51, and 0.64 μm), three near-IR (NIR) (0.86, 1.61, and 2.26 μm), and 10 IR channels [7]. The spatial resolution at the nadir point was 0.5 km for the VIS channel at 0.64 μm, 1 km for the VIS channels at 0.47, 0.51, and 0.86 μm and 2 km for the remaining NIR and all IR channels. AMI can measure FD at intervals of 10 min, and observations for Korea and other target areas can be acquired at intervals of 2.5 min [7]. Table I gives the characteristics of the AMI bands and their atmospheric applications [16].

Fig. 1 shows the study area for the FD region, which includes parts of Asia, Australia, and the Pacific and Indian Oceans.

Fig. 2 shows the spectral response functions (SRFs) of the AMI sensor. Notably, the AMI VIS bands have different bandwidths.

This article used the L1 data in the VIS bands of GK-2A/AMI in 4096 $\times$ 4096 pixels to obtain the D2D-generated AMI VIS band data converted from the original AMI FD L1B observation data. The resampled image data from the AMI FD L1B data was used for this purpose.

For the input data of a DL model, the AMI VIS and IR band data were upscaled to a spatial resolution of 4 km in the numerical array of 4096 $\times$ 4096 pixels because of the hyperbolic tangent activation function in the output layer of U-net [38] encoder-decoder in the Pix2Pix software [37]. The resampled AMI VIS data were converted into RGB image data in Mercator map projections of 0–1 albedo units. The AMI data were obtained from NMSC of the KMA.

TABLE II
CORRELATION COEFFICIENTS BETWEEN 0.47 MICRON BAND AND THE OTHER 10 INPUT BAND

Bands (μm)	Nov. 1 2019	Dec. 1 2019	Jan. 1 2020	Feb. 1 2020	Mar. 1 2020	Apr. 1 2020	May. 1 2020	Jun. 1 2020	Jul. 1 2020	Aug. 1 2020	Sep.1 2020	Oct.1 2020
8.7	0.786	0.73	0.718	0.754	0.8	0.812	0.783	0.719	0.725	0.753	0.814	0.807
10.5	0.798	0.736	0.718	0.763	0.811	0.826	0.797	0.73	0.739	0.77	0.826	0.821
11.2	0.797	0.732	0.716	0.76	0.807	0.824	0.795	0.728	0.736	0.769	0.822	0.82
12.3	0.792	0.727	0.713	0.754	0.796	0.815	0.789	0.721	0.73	0.763	0.815	0.813
7.3	0.676	0.64	0.646	0.664	0.688	0.691	0.669	0.617	0.623	0.638	0.698	0.685
10.5 - 8.7	0.645	0.615	0.625	0.634	0.656	0.652	0.628	0.589	0.597	0.598	0.66	0.649
10.5 - 11.2	0.631	0.608	0.62	0.626	0.65	0.641	0.614	0.58	0.586	0.581	0.648	0.635
10. 5 - 12.3	0.646	0.622	0.632	0.639	0.666	0.657	0.628	0.593	0.598	0.594	0.663	0.651
10.5 - 6.3	0.75	0.702	0.7	0.722	0.759	0.767	0.739	0.682	0.689	0.708	0.772	0.764
10.5 - 7.3	0.764	0.715	0.71	0.732	0.775	0.781	0.75	0.695	0.702	0.719	0.786	0.779

Fig. 1. Study areas of the GK-2A/AMI.

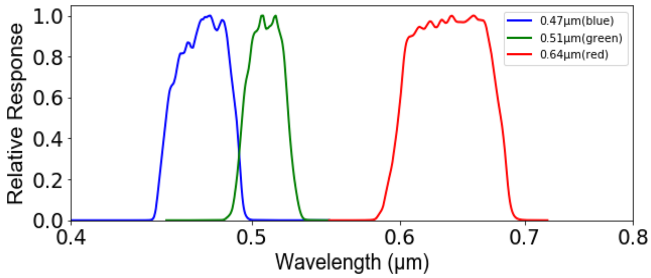

Fig. 2. SRFs of the blue, green, and red bands in the AMI sensor.

B. RGB Composite Imagery

One of the input datasets was AMI RGB data in 0–1 albedo unit as a numerical array (4096 × 4096 × 3 pixels). Notably, a hybrid green band was used for the final outputs of RGB images instead of the AMI green band [39] because of the weak SRF of the green band and realistic green color saturation. The hybrid green band in the AMI RGB data is expressed as [33]

$$R_{\text{hybrid\_Green}} = (1 - F) \cdot R_{\text{Green}} + F \cdot R_{\text{NIR}} \tag{1}$$

where the R_{Green} is the original AMI green band, R_{NIR} is the reflectance at the AMI NIR (0.86 μm) band, and F is the fractional value between 0 and 1. This article used $F = 0.13$, officially employed in the KMA for producing AMI RGB images.

C. Band Selection for Adversarial Learning

Apart from the AMI RGB data with the hybrid green band, input datasets of a D2D model were prepared for adversarial learning. It was assumed that the longwave IR (LWIR) bands of AMI are unaffected by solar reflection. The best pairs of AMI LWIR bands and AMI RGB data were obtained by testing the best correlation coefficients (CC) between the AMI RGB bands and LWIR bands or the differences in the LWIR bands. Table II gives the CC values between the AMI 0.47 μm band and the other selected ten input bands (10.5, 11.2, 12.3, 8.7, and 7.3 μm) or band differences (0.5–12.3, 10.5–11.2, 10.5–8.7, 10.5–6.3, and 10.5–7.3 μm) as a pair of the AMI RGB bands for adversarial learning and developing the D2D model.

D. Preprocessing of Input Datasets For Data-2-Data Translation

For training and testing the D2D model, the pairs of overlapped multiband input datasets (X_R, Y_R) were mathematically expressed as follows:

$$X_R = x_i \in \{\text{AMI}_{\text{IR and }\Delta\text{IR}}\} \tag{2}$$

$$Y_R = y_i \in \{\text{AMI}_{\text{RGB}}\} \tag{3}$$

where the subscript IR is the T_B at IR bands, the subscript ΔIR denotes the T_B difference between two different IR bands observed at the AMI IR bands, the subscript RGB is the AMI RGB data, and the subscript R denotes the real observation.

For preprocessing, all the original L1 datasets observed in the five selected bands and five-band differences of the AMI sensor were converted into normalized numerical datasets in the range [0, 1] as follows [40]:

$$X'_R = \frac{X_R - X_{R,\min}}{X_{R,\max} - X_{R,\min}} \tag{4}$$

$$Y'_R = \frac{Y_R - Y_{R,\min}}{Y_{R,\max} - Y_{R,\min}} \tag{5}$$

with

$$x_{\min} \le x_i \le x_{\max} \in X_R \rightarrow 0 \le x'_i \le 1 \in X'_R \tag{6}$$

$$y_{\min} \le y_i \le y_{\max} \in Y_R \rightarrow 0 \le y'_i \le 1 \in Y'_R \tag{7}$$

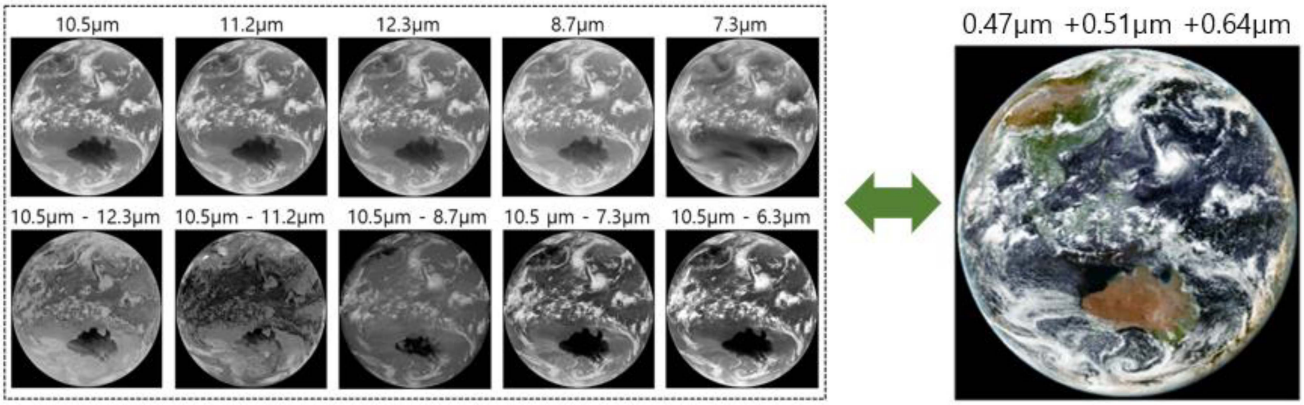

Fig. 3. Example of image pairs at AMI IR bands and differences, and AMI RGB data on September 2, 2020 at 04:00 UTC.

where X'_R and Y'_R are the datasets of the normalized real-observed data x'_i and y'_i, respectively; and $x_{\min}$, $x_{\max}$, $y_{\min}$, and $y_{\max}$ are the minimum and maximum values of the observed data x_i and y_i, respectively.

Thus, we can express the pairs of overlapped multiband input datasets $(X'_R,\ Y'_R)$ for the training and validation of the D2D model as follows:

$$\begin{aligned} X'_R = y'_i \ \in \{&R'_{10.5}, R'_{11.2},\ R'_{12.3},\ R'_{8.7}, R'_{6.3} \\ &R'_{10.5} - R'_{12.3},\ R'_{10.5} - R'_{11.2},\ R'_{10.5} - R'_{8.7} \\ &R'_{10.5} - R_{6.3},\ R'_{10.5} - R'_{7.3}\} \end{aligned} \tag{8}$$

$$Y'_R = x'_i \ \in \{R'_{\text{Blue}},\ R'_{\text{Green}}, R'_{\text{Red}}\} \tag{9}$$

where R' is the normalized albedo or T_B. The subscripts denote the central wavelengths (μm) of the band.

After its development, output datasets of virtual AMI RGB data (Y'_{RGB}) were obtained by applying the D2D model to other input datasets that were not used during training.

For postprocessing, the model output datasets were denormalized as normalized numerical array as follows:

$$Y_V = Y_{R,\min} + Y'_{\text{RGB}} \times (Y_{R,\max} - Y_{R,\min}) \tag{10}$$

where Y_V is the virtual D2D-generated AMI RGB data in 0–1 albedo units in numerical array with a size of (4096 × 4096 × 3). Subscript V denotes a virtual product of the D2D model. Notably, the D2D-generated GK-2A/AMI RGB data are quantitatively translated, different from simple image-to-image translation.

Fig. 3 shows an example of paired images of AMI IR bands and differences as input data for adversarial learning to produce virtual AMI VIS band data.

III. Methods

A. Pix2Pix Model

GANs are generally composed of both generator and discriminator models. The generator (G) in the Pix2Pix model is a mathematical function that generates a virtual output variable (output images) from independent variables (actual input and output images), and can be expressed as follows:

$$Y_V = G\left(X_R, Y_R\right) \tag{11}$$

$$\text{with}\ \ (x_i,\ y_j) \in X_R \times Y_R \ \text{ and } y_k \in\ Y_V =\ G\left(X_R, Y_R\right) \tag{12}$$

where x_i and y_j are the observed input and output image data in the datasets X_R and Y_R. The subscripts i and j denote the number of input image data points in X_R and Y_R , respectively. The subscript k denotes the number of output data points in Y_V. Subscript R denotes the observed data and y_k is the virtual output data produced by the mapping function G.

The discriminator model (D) is a data-scaling function used to discriminate the similarity between the observed (X_R) and virtual output (Y_V) [41]

$$Z\ =\ D\left(Y_R,\ Y_V\right) \tag{13}$$

$$= P(Y_V|Y_R) \tag{14}$$

$$\text{with}\ \ z_l \in Z\ =\ [0,\ 1] \tag{15}$$

where $P(Y_V|Y_R)$ is the conditional probability from 0 to 1 between the observed (Y_R) and the virtual (Y_V) outputs. $P(Y_V|Y_R) = 0$ when Y_V is completely different from Y_R, whereas $P(Y_V|Y_R) = 1$ when $Y_V = Y_R$ [16]. Z is the data scaling result from 0 to 1.

To implement the cGAN method, Pix2Pix [37], [40] uses a loss function (L_{P2P}), combined with adversarial loss ($L_{C\text{GAN}}$) and reconstruction loss (L_1), as follows [16]:

$$L_{P2P} = \min_G \max_D \ \{L_{C\text{GAN}}\} \ + \lambda \cdot L_1 \tag{16}$$

where $\min_G \max_D$ denotes the minimum-maximum function between G and D. λ is the tradeoff parameter between adversarial and reconstruction losses. This article set $\lambda = 1$.

The first term in (16) is the adversarial loss ($L_{C\text{GAN}}$), expressed as follows [42], [43], [44], [45]:

$$\begin{aligned} L_{C\text{GAN}} = \ & E\left[\log\left(D\left(Y_V, Y_R\right)\right)\right] \\ & + E\left[\log\left(1 - D\left(Y_R, G(X_R,\ Y_R)\right)\right)\right] \end{aligned} \tag{17}$$

where X_R and Y_R are pairs of observed input and output data, respectively. The generator minimizes the terms of

$\log(D(Y_V, Y_R))$ in the first cross entropy, whereas the discriminator maximizes the probability of discriminating observed or virtual output data in the second cross entropy. The cross-entropies include a log function compensating the gradient insufficiency at the beginning of the training [45].

The second term in (16) is the reconstruction loss (L_1) [46], which is a traditional standard loss, expressed as follows [37]:

$$L_1(G) = E(\|Y_R - Y_V\|_1) \tag{18}$$

where (18) minimizes the distance between the virtual (Y_V) and the observed (Y_R) output datasets to reduce the blurry effects.

The daytime AMI LWIR bands and differences in the LWIR band data were assigned as X_R, and the daytime AMI IR RGB data were Y_R. Notably, it was assumed, in which the nighttime AMI IR bands resemble the daytime AMI IR bands because of the weak dependence of IR bands on solar effects. Thus, virtual day and night GK-2A/AMI RGB bands (Y_V) were estimated from the constructed D2D model.

B. Model Training, Validation, and Application

Mathematically, the dataset consists of a pair of AMI RGB and IR data, expressed as follows:

$$\text{Input}: \ \{X_R, Y_R\} = \{\text{AMI}_{\text{IR and }\Delta\text{IR}}, \text{AMI}_{\text{RGB}}\} \tag{19}$$

where AMI_{RGB} and AMI_{IR} are the observed AMI RGB and IR data, respectively.

Paired datasets of a sequence array (4096 × 4096 × 10) created by stacking 10 images and in a sequence array (4096 × 4096 × 3) were used as input datasets for the D2D model. The D2D model was trained to resemble the observed AMI RGB bands. The model was reiteratively trained and selected at the iteration step to obtain the best CC and minimum root-mean-square-error (RMSE) between the observed AMI RGB data and D2D-generated virtual AMI RGB data.

The virtual AMI RGB data were generated using different AMI IR data as the input dataset as follows:

$$\{Y_V\} = \{\text{AMI}'_{\text{RGB}} = \text{D2D model}\ (\text{AMI}_{\text{IR and }\Delta\text{IR}})\} \tag{20}$$

where AMI'_{RGB} represents D2D-generated virtual AMI RGB data. Thus, the constructed D2D model was able to produce virtual daytime and nighttime AMI RGB bands that were not available in the AMI observations.

This article used 356 pairs of AMI training datasets at 04:00 UTC from November 1, 2019 to October 31, 2020, and 24 pairs of AMI test datasets at 04:00 UTC on the 1st and 15th of each month from January to December, 2021. The D2D model was trained and tested using TensorFlow with Python 3.7.6 of Linux Ubuntu 16.04.5 on CUDA 10.0 and cuDNN 7.6.5 systems running on four NVIDIA Titan-RTX GPU and an Intel Xeon CPU. Training time of the model was approximately four days.

Fig. 4 demonstrates the procedure of D2D model processing and summarizes the preprocessing, training, testing, and postprocessing. During preprocessing, the input datasets were normalized between 0 and 1. The model was trained using a generator and discriminator. The postprocessing results of the D2D-generated AMI RGB bands were denormalized to the range of the original AMI RGB observations.

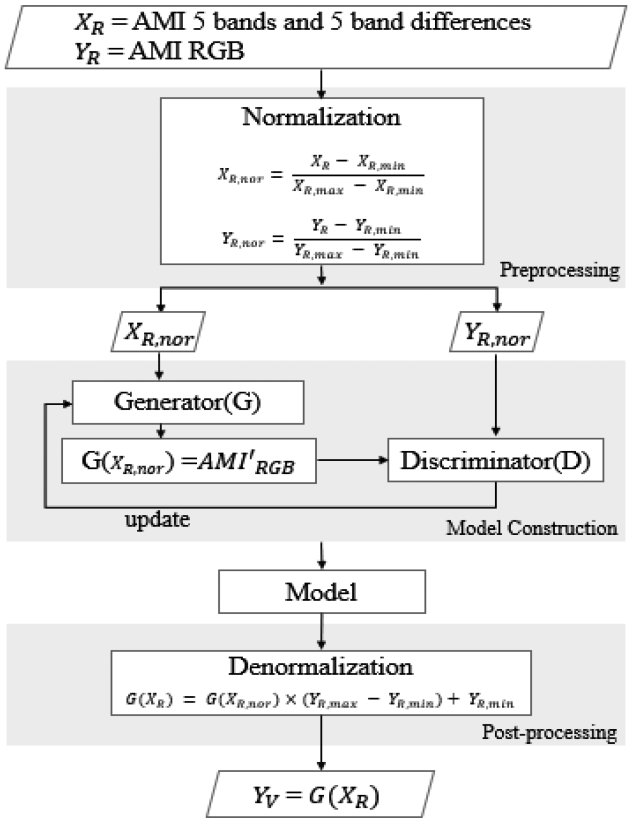

Fig. 4. Schematic of D2D model processing to generate virtual AMI RGB bands from training to application.

C. Statistical Comparison

A statistical comparison was performed between the observed AMI RGB bands and D2D-generated AMI RGB bands. The CC, bias, and RMSE values were as follows [47]:

$$CC = \frac{\sum_{i=1}^{N}\left(Alb_{G,i} - \overline{Alb}\right)\sum_{i=1}^{N}\left(Alb_{G,i} - \overline{Alb_A}\right)}{\sqrt{\sum_{i=1}^{N}\left(Alb_{G,i} - \overline{Alb_G}\right)^2}\sqrt{\sum_{i=1}^{N}\left(Alb_{A,i} - \overline{Alb_A}\right)^2}} \tag{21}$$

$$\text{Bias} = \frac{1}{N}\sum_{i=1}^{N}\left(Alb_{G,i} - Alb_{A,i}\right) \tag{22}$$

$$\text{RMSE} = \sqrt{\frac{1}{N}\sum_{i=1}^{N}\left(Alb_{G,i} - Alb_{A,i}\right)^2} \tag{23}$$

where N is the total number of pixels in the AMI data, i is the index from 1 to N, $Alb_{A,i}$ denotes the $Albedo$ of the ith pixel in the observed AMI data, and $Alb_{G,i}$ denotes the $Albedo$ of ith pixel in the D2D-generated AMI data. $\overline{Alb_A}$ and $\overline{Alb_G}$ are the mean $Albedo$ of the observed and D2D-generated data, respectively.

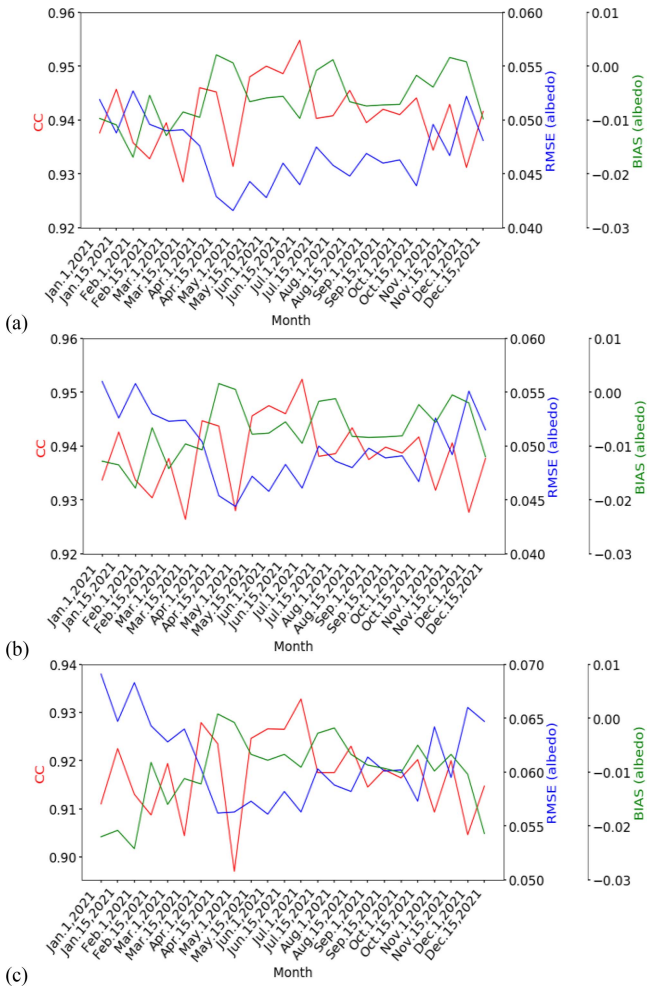

Fig. 5. CC and RMSE validations at (a) blue, (b) green, and (c) red bands between the real and the D2D-generated AMI on 1st and 15th of each month from January to December, 2021 at 04:00 UTC.

IV. Results

A. D2D Model Construction

Fig. 5 shows the results of the variations in CC, RMSE, and bias between the observed and D2D-generated AMI RGB band albedos generated by iterations during the training of the model on 1st and 15th of each month from January to December 2021 at 04:00 UTC. On July 1, 2021, the D2D model showed a maximum CC of 0.947 and minimum RMSE of 0.049. The RMSE values for the AMI blue, green, and red bands were relatively high during winter than summer due to the different seasonal cloud coverages in the full disk. After training, the optimal number of iterations for the blue, green, and red bands was 21 500, which was used to create the virtual RGB albedo GK-2A/AMI sensor.

Table III gives the accuracy of the constructed D2D model with excellent average CC, bias, and RMSE values between the observed and D2D-generated AMI RGB bands.

B. Daytime AMI

Fig. 6 shows the observed and D2D-generated FD RGB images on April 15, 2021, at 04:00 UTC (daytime). These images displayed excellent consistency with the observed AMI RGB images for clouds, oceans, deserts, and vegetation areas.

TABLE III
Statistical Results of the Trained Model Using AMI RGB Bands

Bands	Red	Green	Blue
CC	0.917	0.939	0.941
RMSE (albedo)	0.061	0.050	0.047
BIAS (albedo)	-0.010	-0.007	-0.006

Fig. 7 shows the observed and D2D- generated AMI blue, green, and red bands, and the spatial differences between them. The three VIS bands illustrated the consistent features of clouds, ocean, deserts, vegetation areas, and sun glint effects over the Equator.

Fig. 8 displays the scatterplots between the observed and D2D-generated AMI RGB band albedo with CC $=$ 0.945, bias $=$ 0.002, and RMSE $=$ 0.043 for the blue band, CC $=$ 0.944, bias $=$ 0.002, and RMSE $=$ 0.045 for the green band, and CC $=$ 0.923, bias $=$ 0.001, and RMSE $=$ 0.056 for the red band. Notably, the three bands showed similar accuracies, despite the different spectral bandwidths in the three AMI VIS bands. The proposed D2D model showed a disadvantage in simulating the small fraction of pixels affected by sun glints.

C. Nighttime AMI

Fig. 9 shows the observed and D2D-generated FD RGB images on April 29, 2021, at 16:00 UTC (nighttime). Although nighttime observations were not available, the D2D-generated FD RGB image displayed was as clear as a daytime image under solar reflection. Notably, the sun glint effect was not observed in the virtual RGB image. The D2D-generated FD RGB image displayed similar features of clouds, ocean, deserts, and vegetation areas to the observed daytime AMI RGB image (see Fig. 6). However, the desert area in Australia showed the possibility of clouds, which was incorrect.

Fig. 10 shows the real AMI IR 10.5 μm band images at 04:00 UTC (daytime) and 16:00 UTC (nighttime) on the 29th of January, April July, and October, 2020. Significant differences between daytime and nighttime IR bands existed over the desert area in Australia owing to its high diurnal variation in surface temperatures. These results showed the limitation of the D2D method over desert regions because this article assumed the equivalent observation values of AMI IR bands during the day and night. However, despite the absence of solar effects, desert regions were beyond this assumption.

To correct the unrealistic results over the desert area in Australia, we adjusted the weighting coefficients to the T_B and T_B differences for AMI 8.7, 10.5, 11.2, 12.3 μm bands and 10.5 -6.3, and 10.5–7.3 μm bands. The corrected AMI IR input data were used to train and test the modified D2D model after masking the other regions in the FD area, except for Australia, as follows:

$$T_B \rightarrow T_B \times 0.8 \text{ at } 10.5,\ 11.2,\ \text{and } 12.3\ \mu\text{m bands} \quad (24)$$

$$T_B \rightarrow T_B \times 0.9 \text{ at } 8.7\ \mu\text{m bands} \quad (25)$$

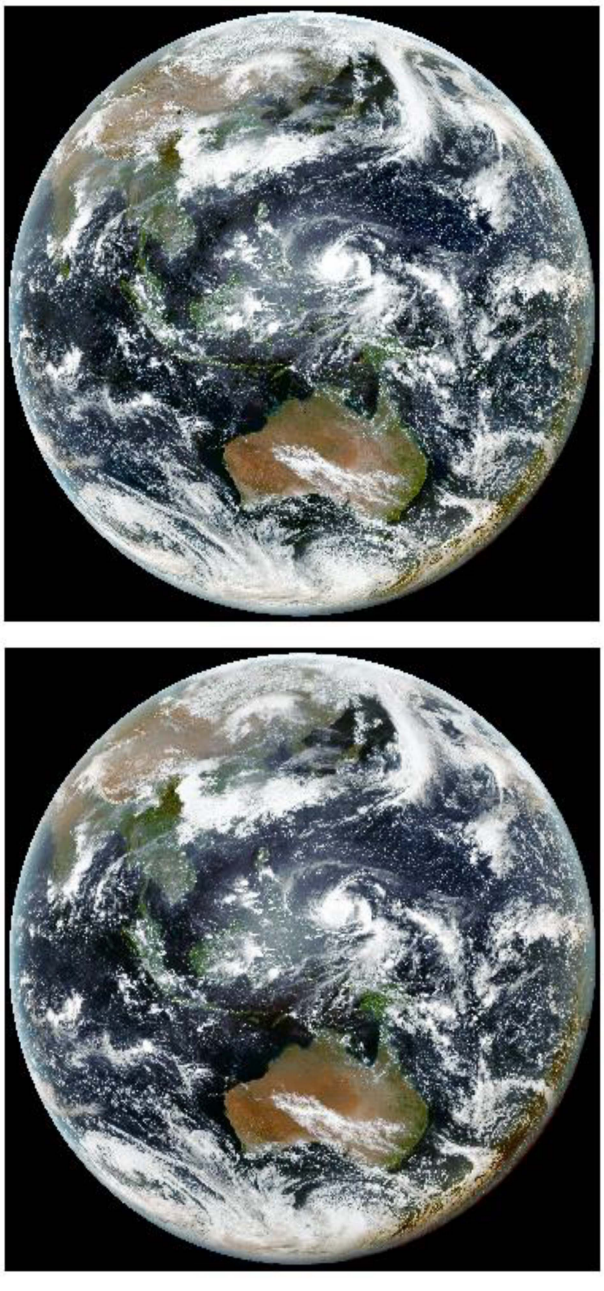

Fig. 6. (a) Observed and (b) D2D-generated AMI RGB images on April 15, 2021, at 04:00 UTC.

$$\Delta T_B \rightarrow \Delta T_B \times 0.75 \ \text{ at } \ 10.5 - 6.3\ \mu\text{m and } \ 10.5 - 7.3\ \mu\text{m}. \tag{26}$$

Fig. 11 shows the results of the modified D2D-generated RGB images at night, which were significantly improved.

V. Discussion

A D2D-based method was proposed to simulate the virtual blue, green, and red bands of the GK-2A AMI sensor with AMI IR bands and their combination based on the assumption of the consistency of LWIR bands during day and night. This article

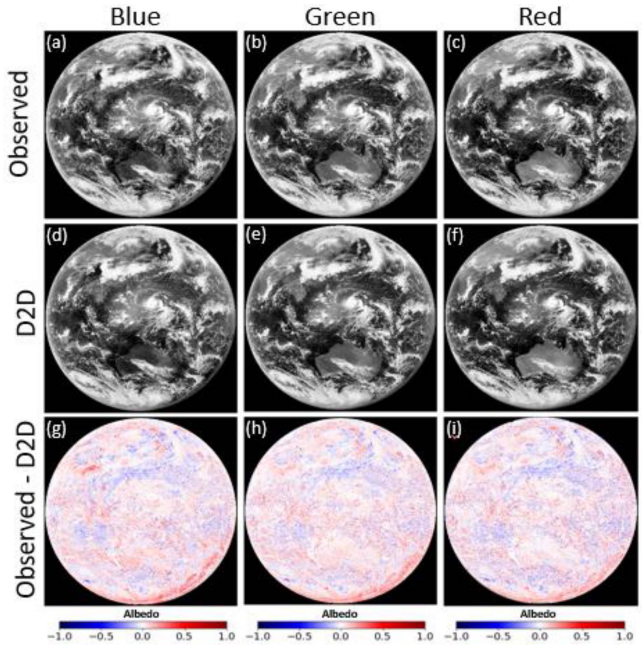

Fig. 7. Observed AMI (a) blue, (b) green, (c) red bands; and D2D-generated (d) blue, (e) green, (f) red bands. Spatial differences between observed and D2D-generated AMI (g) blue, (h) green, and (i) red bands from −1 to 1 albedo. The date is April 15, 2021, at 04:00 UTC, as shown in Fig. 6.

significantly contributes to the geostationary weather satellite information owing to its capability to simulate physically useful information when satellite data are unavailable.

Previously, a virtual red band (0.675 μm) was generated in the COMS/MI sensor [31]. They used pairs of a red band and LWIR (10.8 μm) band of the COMS/MI sensor and obtained CC = 0.88, bias = −2.41 digital number (DN), and RMSE = 36.85 DN during summer, and CC = 0.89, bias = −0.21 DN, and RMSE = 33.02 DN during winter between the observed and cGAN-generated COMS/MI red band [31]. Another study [16] presented a multi-IR band-based cGAN model with improved results (CC = 0.952, bias = −1.752 DN, and RMSE = 26.851 DN) (particularly for the convective clouds and typhoons) compared to the previous single-band CGAN model [31], because of the sounding effects from the IR bands that are sensitive to water atmospheric vapor layers. Notably, this article showed improved results for AMI red band generation with a CC = 0.917, bias = −0.01, and RMSE = 0.061 compared to the previous study [16]. Another study generated a virtual green band for other geostationary weather satellites using advanced baseline imager (ABI) and Advanced Himawari Imager sensors [33]. They compared cGAN-generated and synthetic ABI green bands, and obtained CC = 0.993, bias = 1.029 DN, and RMSE = 2.892 DN. The present article showed improved results of CC = 0.939, bias = −0.007, and RMSE = 0.05 for the AMI green band generation. These improved results were attributed to the D2D translation, which used collocations and various pairs of input datasets in the pairs of satellite RGB and IR bands.

The present article was limited by the absence of a validation data for the D2D-generated virtual nighttime AMI RGB image.

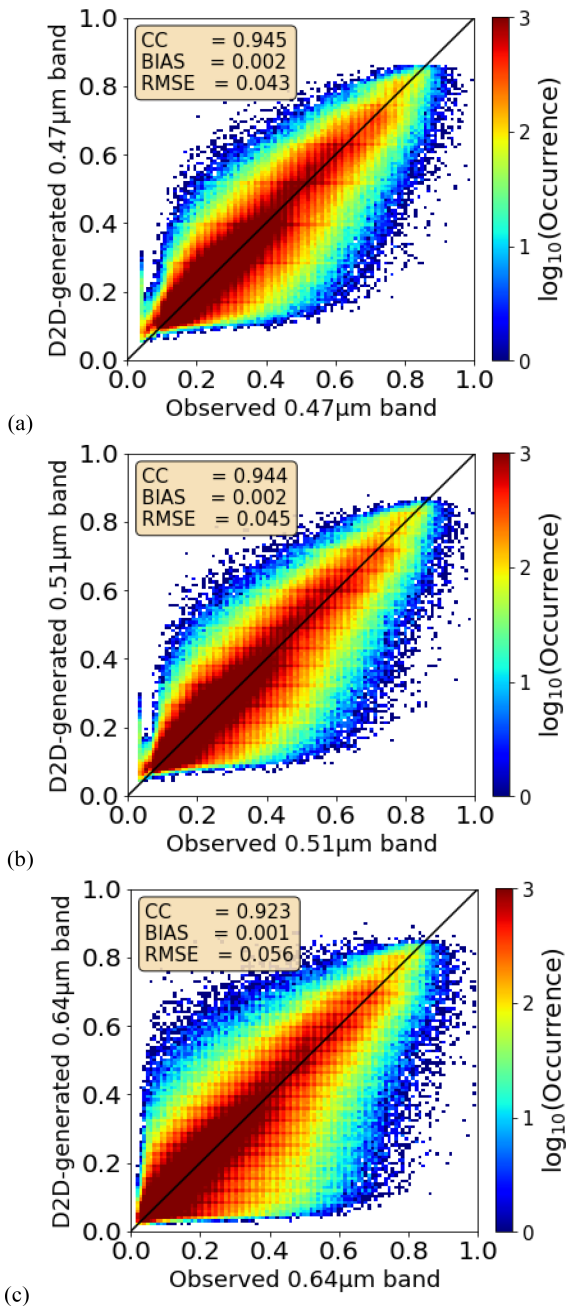

Fig. 8. Scatterplots between the observed and the D2D-generated AMI (a) blue, (b) green, and (c) red bands albedo, respectively. The time is the same as Fig. 6.

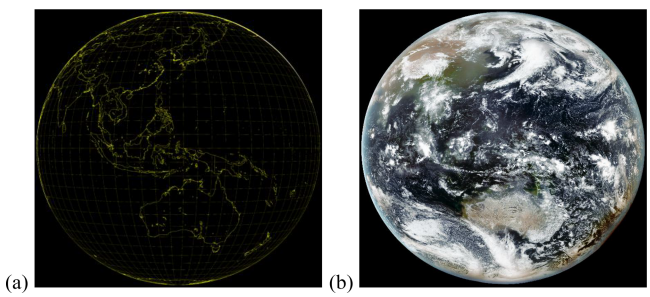

Fig. 9. (a) observed AMI and (b) D2D-generated AMI RGB images on April 29, 2021, at 16:00 UTC.

However, the D2D-based results provided quantitatively reasonable albedos over the FD region in the absence of solar reflection. Thus, D2D-generated virtual nighttime AMI RGB data may be qualitatively validated to analyze the consistent temporal variation of meteorological phenomena, such as cloud movements, vegetation distribution, and sea surface temperatures during the day and night.

The proposed D2D method showed a fundamental limitation in its assumption, which could not be applied to regions with a high daily variation in surface temperature, including desert areas, because of temperature contrasts in the IR bands during the day and night. Thus, the D2D method should be cautiously applied to other geostationary weather satellites, such as the GOES-16, MTG, Himawari-8, and FY-4A, and exclude desert areas. Nevertheless, this article provided an empirical correction method for misidentification of deserts as cloud cover. However, further studies on the weighting coefficients in (24)–(26) should be investigated over various deserts on different continents for different periods because the correction factors have spatiotemporal dependencies.

In addition to the D2D method, hypothetical bands of the GK-2A AMI sensor could be generated using traditional methods based on rigorous radiative transfer (RT) simulation. For example, VIS to IR bands of the Fengyun satellite were simulated using a forward RT model [48]. Furthermore, the proposed D2D model could be improved if the surface albedo and clear-sky reflectance are used as additional input data for training the D2D model. Thus, fast and accurate RT model-based methods could correct unrealistic results over the deserts and validate the D2D-generated virtual nighttime AMI VIS bands for further research.

Despite rapid advances in hardware performance, the GPU memory intensiveness induced an additional limitation in computing the D2D model to generate the FD data with the original high spatial resolution (0.5 km at the red band and 1.0 km at the blue and green bands). Thus, AMI RGB bands were resampled at a spatial resolution of 4 km in a numerical array of 4096×4096 pixels for the AMI FD RGB data. Discontinuous values were observed at the edges of 4096×4096 patches during testing using the original spatial resolution of AMI FD RGB datasets. This issue will also be addressed in future studies.

Despite a few limitations, this article proposed an efficient model to generate VIS RGB data for global regions or time zones without solar reflections using the officially operating GK-2A/AMI sensor. Combined with high the spatiotemporal resolutions of geostationary weather satellites, virtual RGB data can help weather forecasters monitor and predict cloud movements and distributions, weather analysis, and natural disasters, such as typhoons and aerosols, especially in Southeast Asian countries that do not have any weather satellites. The KMA/NMSC currently provides D2D-generated RGB images to the public and worldwide along with the observed AMI RGB data (https://nmsc.kma.go.kr/homepage/html/satellite/viewer/selectSatViewer.do?dataType=operSat). Using traditional satellite remote sensing techniques, this satellite data service would have been impossible.

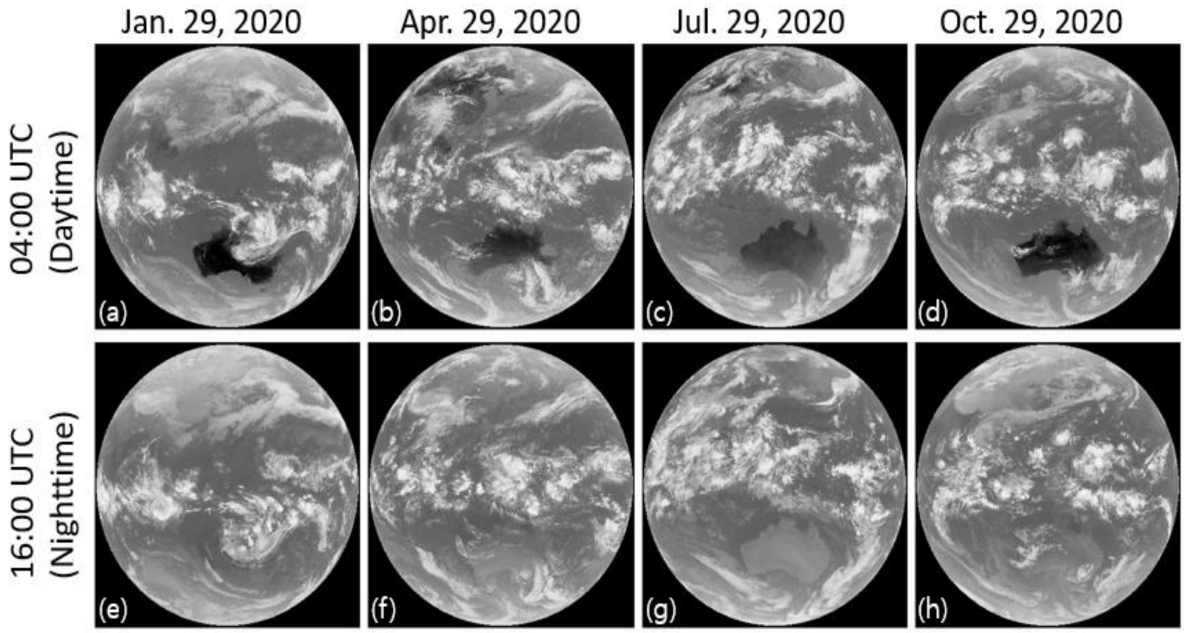

Fig. 10. Observed AMI IR 10.5 μm bands at 04:00 UTC (day time) January 29, (b) April 29, (c) July 29, and (d) October 29, 2020 (a), and 16:00 UTC (nighttime), (e) January 29, (f) April 29, (g) July 29, and (h) October 29, 2020.

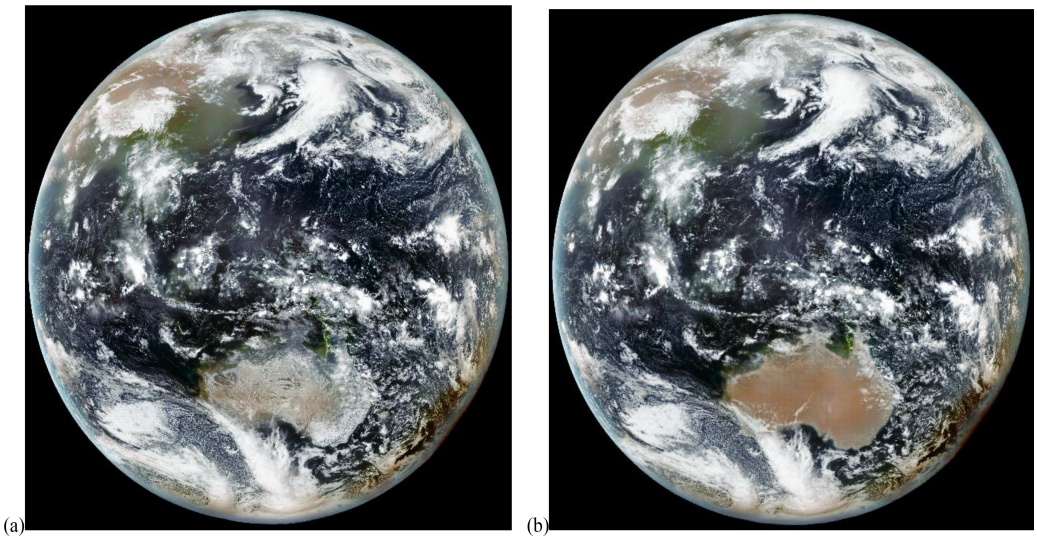

Fig. 11. (a) D2D-generated and (b) modified D2D-generated AMI RGB images, images on April 29, 2021, at 16:00 UTC (nighttime).

This article can be applied to other global geostationary weather satellites, such as GOES-16 and MTG. Three satellites can be combined for simultaneous global monitoring of weather and atmospheric environments.

VI. Summary and Conclusion

Geostationary weather satellites play essential roles in weather analysis during natural disasters, such as typhoons, floods, and heavy rainfall, and those which observe VIS to IR bands are advantageous owing to their relatively high spatiotemporal resolutions. The VIS and IR bands can effectively observe clouds related to different weather phenomena. True-color RGB imagery based on the observations of the VIS band has been particularly helpful for forecasters in this regard because of its intuitive understanding, visualization, and lack of observational data loss, which is different from the *L2* products. However, the use of the VIS band and RGB data depends on the daytime solar reflection.

This article presented a D2D method to generate virtual AMI VIS bands in the region and time zone with no solar reflection using the cGAN technique with paired datasets of the GK-2A/AMI blue, red, and green bands and a combination of IR bands. Notably, the D2D-generated outputs had the same physical

values and ranges as the input datasets. The proposed DL model consisted of three steps: preprocessing of data normalization; cGAN model; and postprocessing of the D2D-generated data denormalization. The D2D model was trained and tested using Linux with four NVIDIA GeForce RTX 2080 Ti and an Intel Xeon CPU.

The daytime D2D-generated AMI VIS band albedos showed an excellent statistical agreement with the observed daytime AMI VIS band albedos. Through an assumption of consistency of LWIR bands during day and night, the daytime D2D model was applied to generate virtual nighttime AMI VIS band albedos translating the nighttime AMI IR bands to the nonexistent daytime AMI VIS band albedos.

Consequently, the proposed DL model was able to supplement global weather analysis and natural disaster monitoring for forecasters and public users with hypothetical VIS and RGB products without solar effects in various geostationary weather satellites.

ACKNOWLEDGMENT

The authors thank anonymous reviewers for helpful and constructive comments on the manuscript.

REFERENCES

[1] J. F. Purdom and W. P. Menzel, "Evolution of satellite observations in the United States and their use in meteorology," *Historical Essays Meteorol. 1919–1995, Amer. Meteor. Soc.*, pp. 99–155, 1996.

[2] J. Schmetz et al., "Supplement to an introduction to meteosat second generation (MSG)," *Bull. Amer. Meteorol. Soc.*, vol. 83, no. 7, pp. 977–992, 2002.

[3] T. J. Schmit, M. M. Gunshor, W. P. Menzel, J. J. Gurka, J. Li, and A. S. Bachmeier, "Introducing the next-generation advanced baseline imager on GOES-R," *Bull. Amer. Meteorol. Soc.,* vol. 86, no. 8, pp. 1079–1096, 2005.

[4] K. Bessho et al., "An introduction to himawari-8/9—Japan's new-generation geostationary meteorological satellites," *J. Meteorol. Soc. Jpn. Ser. II,* vol. 94, no. 2, pp. 151–183, 2016.

[5] J. Yang, Z. Zhang, C. Wei, F. Lu, and Q. Guo, "Introducing the new generation of Chinese geostationary weather satellites, Fengyun-4," *Bull. Amer. Meteorol. Soc.,* vol. 98, no. 8, pp. 1637–1658, 2017.

[6] A. Rodriguez, R. Stuhlmann, S. Tjemkes, D. M. Aminou, H. Stark, and P. Blythe, "Meteosat third generation: Mission and system concepts," in *Proc. Infrared Spaceborne Remote Sens. Instrum. XVII*, 2009, vol. 7453, pp. 88–97.

[7] S. Lyu, "Satellite programs and applications of KMA: Current and future," in *Proc. 6th Asia/Oceania Meteorol. Satell. Users' Conf.*, 2015, pp. 9–13.

[8] Y. Hwang, B.-S. Lee, H.-Y. Kim, J. Kim, H. Kim, and H.-S. Shin, "Communication, ocean, and meteorological satellite orbit determination analysis considering maneuver scheme," in *Proc. AIAA/AAS Astrodyn. Specialist Conf. Exhibit*, 2006, pp. 1648–1660.

[9] D. Kim, M. Gu, T.-H. Oh, E.-K. Kim, and H.-J. Yang, "Introduction of the advanced meteorological imager of Geo-Kompsat-2a: In-orbit tests and performance validation," *Remote Sens.,* vol. 13, no. 7, 2021, Art. no. 1303.

[10] Y.-Y. Choi and M.-S. Suh, "Development of a land surface temperature retrieval algorithm from GK2A/AMI," *Remote Sens.,* vol. 12, no. 18, 2020, Art. no. 3050.

[11] N. Seong, K.-S. Han, K. Lee, and M. Seo, "Estimation NDVI using normalized reflectance through GK-2A/AMI data," in *Proc. AGU Fall Meeting Abstract*, 2019, pp. GC43I–G1465.

[12] E. D. Conway, *An Introduction to Satellite Image Interpretation*. Baltimore, MD, USA: JHU Press, 1997.

[13] Y. Kim and S. Hong, "Convective cloud RGB product and its application to tropical cyclone analysis using geostationary satellite observation," *J. Korean Earth Sci. Soc.*, vol. 40, no. 4, pp. 406–413, 2019.

[14] H. Letu et al., "Investigation of ice particle habits to be used for ice cloud remote sensing for the GCOM-C satellite mission," *Atmos. Chem. Phys.,* vol. 16, no. 18, pp. 12287–12303, 2016.

[15] H. I. Andrews and J. M. Bright, "Evaluating fog detection using himawari-8 satellite imagery and bispectral image processing," in *Proc. Asia Pac. Sol. Res. Conf.*, Sydney, Australia, Dec. 4–6th, 2018.

[16] J.-H. Kim, S. Ryu, J. Jeong, D. So, H.-J. Ban, and S. Hong, "Impact of satellite sounding data on virtual visible imagery generation using conditional generative adversarial network," *IEEE J. Sel. Topics Appl. Earth Observ. Remote Sens.,* vol. 13, pp. 4532–4541, Aug. 2020.

[17] X.-W. Chen and X. Lin, "Big data deep learning: Challenges and perspectives," *IEEE Access*, vol. 2, pp. 514–525, 2014.

[18] J.-G. Lee et al., "Deep learning in medical imaging: General overview," *Korean J. Radiol.*, vol. 18, no. 4, pp. 570–584, 2017.

[19] Y. Tao, K. Hsu, A. Ihler, X. Gao, and S. Sorooshian, "A two-stage deep neural network framework for precipitation estimation from bispectral satellite information," *J. Hydrometeorol.*, vol. 19, no. 2, pp. 393–408, 2018.

[20] C. Chen, X. Chen, and H. Cheng, "On the over-smoothing problem of cnn based disparity estimation," in *Proc. IEEE/CVF Int. Conf. Comput. Vis.*, 2019, pp. 8997–9005.

[21] H.-H. Xu and D.-Y. Ge, "A novel image edge smoothing method based on convolutional neural network," *Int. J. Adv. Robot. Syst.,* vol. 17, no. 3, 2020, Art. no. 1729881420921676.

[22] X. Shi, Z. Chen, H. Wang, D.-Y. Yeung, W.-K. Wong, and W.-C. Woo, "Convolutional LSTM network: A machine learning approach for precipitation nowcasting," in *Proc. Adv. Neural Inf. Process. Syst.*, vol. 28, 2015, pp. 802–810.

[23] E. L. Denton, S. Chintala, and R. Fergus, "Deep generative image models using a Laplacian pyramid of adversarial networks," in *Proc. Adv. Neural Inf. Process. Syst.*, vol. 28, 2015, pp. 1486–1494.

[24] C. N. dos Santos, K. Wadhawan, and B. Zhou, "Learning loss functions for semi-supervised learning via discriminative adversarial networks," 2017, *arXiv:1707.02198*.

[25] A. Radford, L. Metz, and S. Chintala, "Unsupervised representation learning with deep convolutional generative adversarial networks," 2016, *arXiv:1511.06434v2*.

[26] X. Mao, Q. Li, H. Xie, R. Y. Lau, Z. Wang, and S. P. Smolley, "Least squares generative adversarial networks," in *Proc. IEEE Int. Conf. Comput. Vis.*, 2017, pp. 2794–2802.

[27] A. Odena, C. Olah, and J. Shlens, "Conditional image synthesis with auxiliary classifier GaNS," in *Proc. Int. Conf. Mach. Learn.*, 2017, pp. 2642–2651.

[28] J.-Y. Zhu, T. Park, P. Isola, and A. A. Efros, "Unpaired image-to-image translation using cycle-consistent adversarial networks," in *Proc. IEEE Int. Conf. Comput. Vis.*, 2017, pp. 2223–2232.

[29] T. Kim, M. Cha, H. Kim, J. K. Lee, and J. Kim, "Learning to discover cross-domain relations with generative adversarial networks," in *Proc. Int. Conf. Mach. Learn.*, 2017, pp. 1857–1865.

[30] C. Li and M. Wand, "Precomputed real-time texture synthesis with markovian generative adversarial networks," in *Proc. Eur. Conf. Comput. Vis.*, 2016, pp. 702–716.

[31] K. Kim et al., "Nighttime reflectance generation in the visible band of satellites," *Remote Sens.,* vol. 11, no. 18, 2019, Art. no. 2087.

[32] Y. Kim and S. Hong, "Deep learning-generated nighttime reflectance and daytime radiance of the midwave infrared band of a geostationary satellite," *Remote Sens.,* vol. 11, no. 22, 2019, Art. no. 2713.

[33] J.-E. Park, G. Kim, and S. Hong, "Green band generation for advanced baseline imager sensor using pix2pix with advanced baseline imager and advanced himawari imager observations," *IEEE Trans. Geosci. Remote Sens.,* vol. 59, no. 8, pp. 6415–6423, Aug. 2021.

[34] J.-C. Jang, E.-H. Sohn, and K.-H. Park, "Estimating hourly surface solar irradiance from GK2A/AMI data using machine learning approach around Korea," *Remote Sens.*, vol. 14, no. 8, 2022, Art. no. 1840.

[35] J. Lee, M. Kim, J. Im, H. Han, and D. Han, "Pre-trained feature aggregated deep learning-based monitoring of overshooting tops using multi-spectral channels of GeoKompsat-2A advanced meteorological imagery," *GISci. Remote Sens.,* vol. 58, no. 7, pp. 1052–1071, 2021.

[36] H.-Y. Yu, M.-S. Suh, and S.-O. Ryu, "Improvement of thunderstorm detection method using GK2A/AMI, RADAR, lightning, and numerical model data," *Korean J. Remote Sens.,* vol. 37, no. 1, pp. 41–55, 2021.

[37] Y.-C. Lin, "pix2pix-tensorflow," Sep. 10, 2017. [Online]. Available: https://github.com/yenchenlin/pix2pix-tensorflow

[38] O. Ronneberger, P. Fischer, and T. Brox, "U-net: Convolutional networks for biomedical image segmentation," in *Proc. Int. Conf. Med. Image Comput. Comput.-Assist. Intervention*, 2015, pp. 234–241.

[39] S. D. Miller et al., "A sight for sore eyes: The return of true color to geostationary satellites," *Bull. Amer. Meteorol. Soc.*, vol. 97, no. 10, pp. 1803–1816, 2016.

[40] N. Hayatbini et al., "Conditional generative adversarial networks (cGANs) for near real-time precipitation estimation from multispectral GOES-16 satellite imageries—PERSIANN-cGAN," *Remote Sens.*, vol. 11, no. 19, 2019, Art. no. 2193.

[41] B. R. Kiran, D. M. Thomas, and R. Parakkal, "An overview of deep learning based methods for unsupervised and semi-supervised anomaly detection in videos," *J. Imag.*, vol. 4, no. 2, 2018, Art. no. 36.

[42] I. Goodfellow et al., "Generative adversarial nets," in *Proc. Adv. Neural Inf. Process. Syst.*, 2014, pp. 2672–2680.

[43] P. Isola, J.-Y. Zhu, T. Zhou, and A. A. Efros, "Image-to-image translation with conditional adversarial networks," in *Proc. IEEE Conf. Comput. Vis. Pattern Recognit.*, 2017, pp. 1125–1134.

[44] M. Mirza and S. Osindero, "Conditional generative adversarial nets," 2014, *arXiv:1411.1784*.

[45] V. Nguyen, T. F. Yago Vicente, M. Zhao, M. Hoai, and D. Samaras, "Shadow detection with conditional generative adversarial networks," in *Proc. IEEE Int. Conf. Comput. Vis.*, 2017, pp. 4510–4518.

[46] D. Michelsanti and Z.-H. Tan, "Conditional generative adversarial networks for speech enhancement and noise-robust speaker verification," in *Proc. Interspeech*, 2017, pp. 2008–2012.

[47] W. Venables and B. Ripley, "Univariate statistics," in *Modern Applied Statistics With S-PLUS*. New York, NY, USA: Springer, 1999, pp. 113–148.

[48] B. Yao et al., "An accurate and efficient radiative transfer model for simulating all-sky images from Fengyun satellite radiometers," *Sci. China Earth Sci.*, vol. 63, pp. 1701–1713, 2020.